RSC Advances

PAPER

View Article Online
View Journal | View Issue

Cite this: *RSC Adv.*, 2026, **16**, 25717

Facile construction of p–n heterojunction Bi_2O_3/BNNS for synergistic tetracycline removal through adsorption–photocatalysis

Zhao Du, *[a] Yanan Wu,[c] Mengmeng Yu,[a] Zishuang Cheng,[d] Po Hu,[a] Zhonglu Guo,[b] Guifeng Chen,[b] Chengchun Tang[b] and Yi Fang *[b]

Herein, porous boron nitride nanosheets (BNNS) exhibiting n-type semiconductor characteristics were synthesized *via* high-temperature pyrolysis. Subsequently, a series of Bi_2O_3/BNNS composites with superior photocatalytic activity were constructed using a solvothermal method. Experimental results demonstrate that the optimized composite photocatalyst exhibits significantly enhanced adsorption capacity and photocatalytic activity compared to pristine BNNS and Bi_2O_3. The optimal Bi_2O_3/BNNS composite achieved degradation efficiencies of 94.65%, 94.23%, and 93.97% for tetracycline (TC), oxytetracycline (OTC), and doxycycline (DC) (each at 50 mg L^{-1}), respectively, under simulated solar irradiation. This study highlights that the exceptional adsorption capability of BNNS enables the Bi_2O_3/BNNS composite to fulfill the requirements for synergistic adsorption–photocatalysis. Furthermore, BNNS serves as an effective growth substrate, significantly regulating the growth of Bi_2O_3 nanowires and suppressing their agglomeration, thereby endowing the composite with a large specific surface area and pore volume. The formation of a p–n heterojunction also effectively suppresses the recombination of photogenerated charge carriers within the catalyst. Finally, this work elucidates the detailed process and underlying mechanism of photocatalytic tetracycline degradation driven by simulated sunlight. In summary, this study innovatively employs the Bi_2O_3/BNNS composite as a novel photocatalyst for tetracycline degradation and provides theoretical guidance for the design of advanced photocatalysts.

Received 25th March 2026
Accepted 8th May 2026

DOI: 10.1039/d6ra02440h

rsc.li/rsc-advances

1. Introduction

Tetracycline (TC), as one of the most extensively used antibiotics in the world, is widely applied in agriculture and animal husbandry. However, the absorption rate of TC by humans or animals is only 20–30%.[1–3] A large amount of undecomposed TC will be discharged into the natural environment through various channels, which leads to an increase in the drug resistance of pathogens. This eventually poses a potential risk to the stability of the ecosystem. Photocatalytic technology can utilize sunlight to effectively break down antibiotics into H_2O, CO_2, and other small molecules.[4] However, the low efficiency of photocatalytic in practical applications prevents its large-scale application. Adsorption method is another safe and simple method of antibiotic treatment, while taking into account the advantages of high efficiency.[5,6] However, this method can only transfer antibiotics from the water to the surface of the adsorbent but cannot completely eliminate the hazards of antibiotics. Therefore, it also has certain limitations in practical application. In order to overcome the above difficulties, the concept of adsorption–photocatalytic synergistic technology has been proposed.[7–9] The design of multifunctional materials, which possess both efficient adsorption and excellent photocatalytic ability, has become one of the directions to achieving efficient removal for tetracycline pollutants.

Nowadays, metal oxide semiconductors exhibit obvious advantages in the field of photocatalytic degradation. Bismuth-based semiconductor materials are considered to be an ideal class of photocatalysts due to their advantages such as narrower bandgap, less toxicity, and relatively low cost.[10,11] In recent years, bismuth-based semiconductor materials, like Bi_2MoO_6, $BiVO_4$, Bi_2O_3, $Bi_2O_2CO_3$, and so on, have been researched more. It is worth mentioning that the hybridization phenomenon between the orbitals of O 2p and Bi $6s^2$ in Bi_2O_3 leads to the upward shift of its valence band (VB). Therefore, Bi_2O_3 possesses a high oxidation potential and has gained more attention in the field of photocatalytic degradation.[12] Currently, there are six main crystal morphologies of Bi_2O_3: α-Bi_2O_3, β-Bi_2O_3, γ-Bi_2O_3, δ-Bi_2O_3, ε-Bi_2O_3 and ω-Bi_2O_3.[13] Among them, β-Bi_2O_3, with a narrower forbidden bandwidth (~2.3 eV) and

[a]*Provincial Key Laboratory of Intelligent Lighting, Huanghuai University, Zhumadian 463000, China. E-mail: hebutdz@163.com*
[b]*Hebei Key Laboratory of Boron Nitride Micro and Nano Materials, Hebei University of Technology, Tianjin 300130, China. E-mail: fangyi@hebut.edu.cn*
[c]*College of Energy Engineering, Huanghuai University, Zhumadian 463000, China*
[d]*School of Mathematics and Physics, Jingchu University of Technology, Jingmen 448000, China*

stable structure, has been demonstrated to be a p-type semiconductor catalyst that can be excited by visible light.[14] However, β-Bi_2O_3 also faces the same defect of rapid carrier recombination during photocatalysis. In addition, the β-Bi_2O_3, which has a low-dimensional nanostructure, shows better application prospects in photocatalysis due to its higher specific surface area and other factors. However, low-dimensional β-Bi_2O_3 also faces the problem of rapid recombination of photogenerated carriers, as well as severe aggregation phenomena, which greatly limits its photocatalytic capability and further development in the field of photocatalysis. In response to these challenges, researchers have proposed various optimization strategies. Among them, constructing the heterostructure can leverage the synergistic effects between different materials to enhance catalytic activity, which is considered one of the ideal modification methods.[15–17]

Hexagonal boron nitride (h-BN) has a stratified constitution akin to graphite, with each layer consisting of numerous hexagonal rings arranged in a regular pattern. Within each hexagonal ring, the atoms of boron (B) and nitrogen (N) alternate their positions, linked by the sublime bond of B–N covalence.[18,19] These layers are united by the van der Waals. Due to the difference in electronegativity between B and N atoms, the B–N bond, despite being a polar covalent bond, exhibits a certain degree of ionic character.[20] This endows h-BN with excellent chemical stability, high-temperature stability, and adsorption properties. Currently, some studies have demonstrated that h-BN can effectively inhibit the aggregation of surface nanoparticles, enhance the transfer rate of photogenerated carriers in semiconductor materials, and promote the polarization of tetracycline molecules.[21] In addition, h-BN, as a non-metallic material, also meets the requirements of photocatalytic technology with its unique environmental friendliness and cost-effectiveness. Porous BN not only possesses the unique physicochemical properties of h-BN, but also its special microstructure shows enormous potential in the field of antibiotic adsorption. Liu *et al.*[22] successfully synthesized porous BNNS with high specific surface area by calcining the precursor formed by boron trioxide (B_2O_3) and guanidine hydrochloride (CH_6ClN_3) in hydrogen and nitrogen atmospheres, which demonstrated the excellent adsorption performance of porous BNNS towards tetracycline under different pH conditions. Li *et al.*[23] used P123 as a structure-directing agent to synthesize a novel porous BN through a two-step method. The porous BN possesses a multimodal micro/mesoporous structure and abundant surface functional groups, allowing for rapid and efficient adsorption of tetracycline molecules in the environment. Song *et al.*[24] have demonstrated that BN fibers with abundant pore structure possess much higher adsorption capacity for antibiotics compared to commercial BN. Furthermore, it has been substantiated through research that porous BN exhibits the characteristics of an n-type semiconductor.[25] However, the excessive presence of defect structures in porous BN makes it highly susceptible to the trapping of photogenerated carriers, thereby resulting in an inadequate level of photocatalytic activity. Considering that porous BN can not only suppress the aggregation of low-dimensional Bi_2O_3, but also construct a p–n junction with Bi_2O_3. Therefore, theoretically, the composite of Bi_2O_3 and porous BN can satisfy the requirements of adsorption–photocatalytic synergistic effect.

Therefore, based on the above discussion, and in contrast to previously reported Bi_2O_3/BN quantum sheet composites,[26] this study synthesized two-dimensional porous BN nanosheets (BNNS) with micron-sized lateral dimensions and a wrinkled surface through a high-temperature pyrolysis method. Afterward, one-dimensional β-Bi_2O_3 nanowires were grown *in situ* on the surface of BNNS using the solvothermal method, giving rise to a unique "velvet-like" Bi_2O_3/BNNS p–n junction heterostructure that has not been previously reported. The experiment results indicate that the Bi_2O_3/BNNS composites exhibit excellent tetracycline removal ability under simulated sunlight. This enhanced performance is mainly attributed to the strong adsorption capacity of BNNS for tetracycline and the effective induction of the p–n junction that separates the photogenerated charge carriers in Bi_2O_3/BNNS composites. In addition, this work also involves the use of various characterization techniques to conduct in-depth research on the photocatalytic mechanism of Bi_2O_3/BNNS composites and the photocatalytic degradation process of tetracycline.

2. Experimental section

2.1 Materials

Boric acid (H_3BO_3, 99.9%, Aladdin Biochemical Technology Co., Ltd), urea (CH_4N_2O, 99.9%, Aladdin Biochemical Technology Co., Ltd), bismuth nitrate pentahydrate ($Bi(NO_3)_3 \cdot 5H_2O$, 99.9%, Macklin Biochemical Co., Ltd), *N*,*N*-dimethylformamide (C_3H_7NO, AR, Tianjin Kemiou Chemical Reagent Co., Ltd), terephthalic acid ($C_8H_6O_4$, 99%, Macklin Biochemical Co., Ltd), ethanol absolute (C_2H_6O, 99.5%, Tianjin Fengchuan chemical Reagent Co., Ltd), tetracycline (TC), doxycycline (DC) and oxytetracycline (OTC) were obtained from BBI Life Science. The chemicals were utilized without undergoing any additional purification processes.

2.2 Synthesis of BNNS

BNNS were prepared *via* a two-step method. Firstly, weigh a certain amount of boric acid (H_3BO_3) and urea (CH_4N_2O) (molar ratio = 1 : 48) and disperse them in a beaker containing 200 mL of pure water. Afterward, heat the mixed solution in a water bath at 70 °C until the water completely evaporates, resulting in the formation of a white powdered precursor. Finally, the precursor is calcined at 1100 °C in nitrogen gas for 4 hours to obtain BNNS powder.

2.3 Synthesis of Bi_2O_3/BNNS composites and Bi_2O_3 nanowire

In a typical synthesis of Bi_2O_3/BNNS composites, a certain amount of BNNS was added to 50 mL of C_3H_7NO solution and dispersed using ultrasonic waves for 30 min. Then, 0.5 mmol $Bi(NO_3)_3 \cdot 5H_2O$ and 0.1 mmol $C_8H_6O_4$ were added into the mentioned solution and stirred for 30 min. Afterward, incubated the mixed solution at 150 °C for 12 h. After cooling to room temperature, the precipitate was washed with C_3H_7NO

and anhydrous ethanol to obtain the precursor. Finally, Bi_2O_3/BNNS composites were synthesized by calcining at 200 °C in the air atmosphere for 4 hours. The composites with Bi_2O_3 content of 10, 15, 20, 25 and 30 wt% are named Bi_2O_3/BNNS-x (x = 1, 2, 3, 4, and 5), respectively.

The preparation process of Bi_2O_3 nanowires was similar to Bi_2O_3/BNNS composites, with the difference that the addition of BNNS was not required.

2.4 Catalysts characterization

The X-ray diffraction (XRD) technique using a D8-advance instrument from Bruker, operating at 40 kV with a Cu Kα radiation source, was employed to determine the physical phase composition and crystal structure of the catalyst. Fourier transform infrared spectroscopy (FT-IR) with a VECTOR22 spectrometer, covering a wavenumber range of 4000–400 cm^{-1}, was utilized to analyze the chemical bonds and surface functional groups present in the samples. The surface elements of the catalyst were measured by X-ray photoelectron spectroscopy (XPS, ESCALAB 250Xi). The catalyst was analyzed for morphology using scanning electron microscopy (SEM, Quanta 450FEG, FEI) and transmission electron microscopy (TEM, Talos F200S, FEI). The N_2 adsorption–desorption isotherm of the catalyst was characterized by Autosorb iQ at 77 K in liquid nitrogen. The UV-vis diffuse reflectance spectra (UV-vis DRS) were obtained by utilizing a UV-vis spectrophotometer (U-3900H, 240–800 nm) to investigate the light absorption characteristics and band gap of the catalyst. The photoluminescence spectra and fluorescence lifetimes of the catalysts were obtained with fluorescence spectrophotometer (F-4500) and steady-state transient fluorescence spectrometer (fluorog-3 join-yvon spectrophotometer), respectively. The composition of the tetracycline solution was analyzed by liquid chromatography-mass spectrometry (LC-MS, Compact, Bruker Scientific Instruments).

2.5 Photocatalytic activity

The photocatalytic degradation of tetracycline antibiotics was modeled to investigate the photocatalytic activity of the catalysts, in which the antibiotic species included tetracycline hydrochloride (TC), oxytetracycline hydrochloride (OTC), and doxycycline hyclate (DC), all at concentrations of 50 mg L^{-1}. Photocatalytic degradation experiments were conducted in a quartz reactor that allows for the circulation of condensed water. The volume of the antibiotic solution and the mass of the catalyst utilized during the photocatalytic degradation experiments were 100 mL and 20 mg, respectively. Before photocatalytic degradation, the antibiotic solution dispersed with the catalyst was first stirred under dark conditions for 60 min to reach the adsorption equilibrium state. The reactor was then placed under a 300 W Xe lamp to keep the light source about 20 cm from the bottom of the reactor and kept the light for 120 min. During the reaction, 5 mL of the suspension was collected and centrifuged every 20 min, after which the UV-vis absorption spectra of the supernatant were measured. Based on the changes in the absorption intensity of the characteristic peaks, the degradation efficiency of the catalyst for antibiotics can be calculated by eqn (2-1):

$$\text{Degradation rate } \% = 1 - \frac{C_t}{C_0} \times 100\% = 1 - \frac{A_t}{A_0} \times 100\% \quad (2\text{-}1)$$

where C_t and C_0 denote the concentration of the antibiotic solution at light times t and 0, respectively, and A_t and A_0 are the absorption intensities of the characteristic antibiotic absorption peaks at light times t and 0, respectively.

2.6 Electrochemical measurements

The photogenerated current curves, electrochemical impedance spectra, and Mott–Schottky plots of various catalysts were evaluated using a three-electrode system on the CEI670 electrochemical workstation. ITO conductive glass, coated with the catalyst, served as the working electrode, while a Pt electrode and an Ag/AgCl electrode functioned as the counter and reference electrodes, respectively. The preparation of the working electrode involved several steps: initially, a specific quantity of catalyst, PVDF, and anhydrous ethanol was thoroughly ground in a mortar. The resultant mixture was then uniformly applied onto the conductive glass substrate. Subsequently, the coated glass was placed in an oven at 60 °C for 12 hours to eliminate excess solvent and ensure the formation of a stable catalyst film. For the electrochemical performance tests, a 0.5 M Na_2SO_4 solution was utilized as the electrolyte.

3. Results and discussions

The crystal structure and composition of the synthesized Bi_2O_3 nanowires, BNNS, and composites were analyzed using XRD, as illustrated in Fig. 1a. Bi_2O_3 is known to exhibit six distinct crystalline structures. The Bi_2O_3 nanowires produced in this study displayed diffraction peaks at 2θ = 28.0°, 30.8°, 31.8°, 32.8°, 46.3°, 54.5°, and 55.6°, corresponding to the (201), (211), (002), (222), (400), (203), and (421) planes of β-Bi_2O_3 (JCPDS No. 27-0050).[27] In contrast, for the BNNS, clear diffraction peaks attributed to h-BN (JCPDS No. 34-0421) were identified at the (002) and (100) planes, located at 25.8° and 42.5°, respectively.[28] In contrast to the ultrathin BN synthesized through the ball milling method, the X-ray diffraction peaks of BNNS exhibit a broader profile, indicating that BNNS has a relatively lower degree of crystallinity and a higher density of defect structures. Additionally, shifts in the diffraction peak positions confirmed the incorporation of dopant elements such as oxygen and carbon within the BNNS structure. In the XRD spectrum of the Bi_2O_3/BNNS, both Bi_2O_3 and BNNS characteristic diffraction peaks were distinctly observed. The intensity of the Bi_2O_3 peaks increased with higher Bi_2O_3 content, demonstrating the successful fabrication of the composites. Notably, the full width at half maximum (FWHM) of the Bi_2O_3 diffraction peaks in the composite was narrower than pure Bi_2O_3, indicating that BNNS acts as an effective growth matrix, enhancing the crystallinity of Bi_2O_3. Furthermore, strong interactions between Bi_2O_3 and BNNS resulted in slight shifts in the diffraction peaks of BNNS.[29]

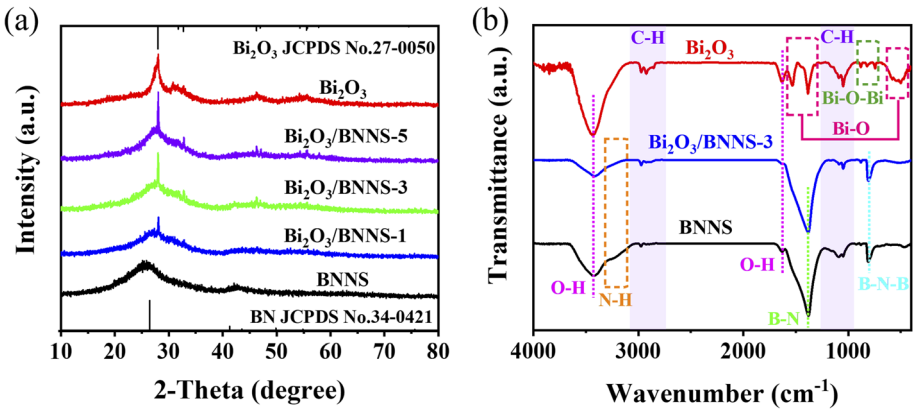

Fig. 1 (a) XRD patterns of Bi_2O_3, BNNS and Bi_2O_3/BNNS composites; (b) FT-IR spectra of Bi_2O_3, BNNS and Bi_2O_3/BNNS-3.

The investigation aimed to analyze the functional groups and chemical bonds present in Bi_2O_3, BNNS, and Bi_2O_3/BNNS through FT-IR analysis. In Fig. 1b, a prominent peak at approximately 3400 cm^{-1} is observed for Bi_2O_3, BNNS, and Bi_2O_3/BNNS-3, indicating the existence of O–H bonds on the material surfaces. Additionally, absorption bands ranging from 2820 to 3000 cm^{-1} and 950–1200 cm^{-1} are associated with C–H bond vibrations, suggesting a significant presence of –OH on all material surfaces alongside internal carbon elements. Furthermore, an absorption band corresponding to the N–H bond is detected between 3050 and 3260 cm^{-1} for BNNS, indicating the generation of amino groups on the surface during precursor pyrolysis.[30] These amino groups serve as plentiful hydrogen-bonding ligands, facilitating the formation of a heterojunction between BNNS and Bi_2O_3. In the case of the Bi_2O_3/BNNS blend, absorption peaks at 425–640 cm^{-1} and 1285–1580 cm^{-1} are related to the Bi–O bonds present within the BiO_6 octahedra, while the peak at 717–909 cm^{-1} corresponds to Bi–O–Bi stretching vibrations.[31,32] Moreover, Bi_2O_3/BNNS-3 displays distinctive absorption bands typical of Bi_2O_3 and additional peaks at approximately 803 and 1380 cm^{-1}, representing B–N–B interlayer bending and B–N intralayer stretching vibrations respectively. This observation confirms the successful synthesis of Bi_2O_3/BNNS and indicates that the inclusion of BNNS does not impact the chemical structure of Bi_2O_3.

To perform a comprehensive analysis of the surface elemental composition and chemical states of Bi_2O_3, BNNS, and the Bi_2O_3/BNNS, XPS spectra of samples were measured and analyzed. The binding energies of the various elements were calibrated using the C 1s peak at 284.8 eV as a reference. The full XPS spectra for Bi_2O_3, BNNS, and Bi_2O_3/BNNS-3 (Fig. 2a) reveal that the surface of the composites comprises five elements: Bi, O, C, B, and N, with no detectable impurity elements present. Fig. 2b presents the high-resolution XPS spectra for Bi 4f in both Bi_2O_3 and Bi_2O_3/BNNS-3. The two characteristic peaks observed correspond to Bi $4f_{5/2}$ and Bi $4f_{7/2}$, both exhibiting an energy level difference of 5.3 eV for these materials. Notably, the binding energies of Bi $4f_{5/2}$ and Bi $4f_{7/2}$ in Bi_2O_3 are elevated, recorded at 164.4 eV and 159.1 eV, respectively. In contrast, the binding energies for the composites are slightly lower, measuring 164.2 and 158.9 eV for Bi $4f_{5/2}$ and Bi $4f_{7/2}$. The high-resolution XPS spectra of the C 1s for Bi_2O_3 and BNNS-3 (Fig. 2c) reveal three characteristic peaks. The peak at 284.8 eV is attributed to the C–C bonds from impurity carbon sources. In Bi_2O_3, the peaks at 288.3 eV and 285.8 eV correspond to C–O bonds and Bi–C bonds, indicating the introduction of a small amount of carbon during the preparation process of Bi_2O_3.[33] Similarly, in Bi_2O_3/BNNS-3, the binding energies of the C–O and Bi–C bonds (288.1 eV and 285.6 eV) are smaller than those in Bi_2O_3. The high-resolution XPS spectra of the B 1s and N 1s for BNNS and Bi_2O_3/BNNS-3 (Fig. 2d and e) reveal characteristic peaks of BNNS at 192.6 eV, 190.5 eV, and 398.1 eV, corresponding to B–O, B–N, and N–B bonds, respectively. However, the binding energies of the B–O, B–N, and N–B bonds in the composites (192.8 eV, 190.7 eV, and 398.3 eV) surpass those in BNNS. A comparison of the high-resolution O 1s XPS spectra of Bi_2O_3, BNNS, and Bi_2O_3/BNNS-3 (Fig. 2f) reveals that the two fitted peaks in Bi_2O_3 correspond to Bi–O bonds (529.9 eV) and surface chemically adsorbed oxygen (531.4 eV). Meanwhile, a characteristic peak for the B–O bond is observed at 532.5 eV in BNNS. Conversely, the binding energy of the B–O bond (532.7 eV) surpasses that present in BNNS. This phenomenon reveals the strong interaction between Bi_2O_3 and BNNS, which drives the electron transfer within the system. As electrons transfer from BNNS and accumulate on the surface of Bi_2O_3, the charge distribution at the interface is reconfigured, thereby forming a built-in electric field. This series of processes confirms the formation of the heterojunction structure.[34]

Fig. 3 displays the SEM and TEM micrographs of Bi_2O_3, BNNS and Bi_2O_3/BNNS. Bi_2O_3 exhibits a uniform one-dimensional fibrous structure with a high aspect ratio, alongside noticeable aggregation tendencies. Contrary to SEM findings, the TEM image reveals that the length of Bi_2O_3 is approximately 100 nm, while the diameter remains around 30 nm. This could stem from the instability in the structure of Bi_2O_3 nanowires, leading to structural disruptions under extended ultrasonication. Fig. 3b and e exhibit the SEM and TEM micrographs of BNNS, depicting an ultra-thin, graphene-like layered configuration with abundant surface creases. Such a morphology grants BNNS a sizable specific surface area,

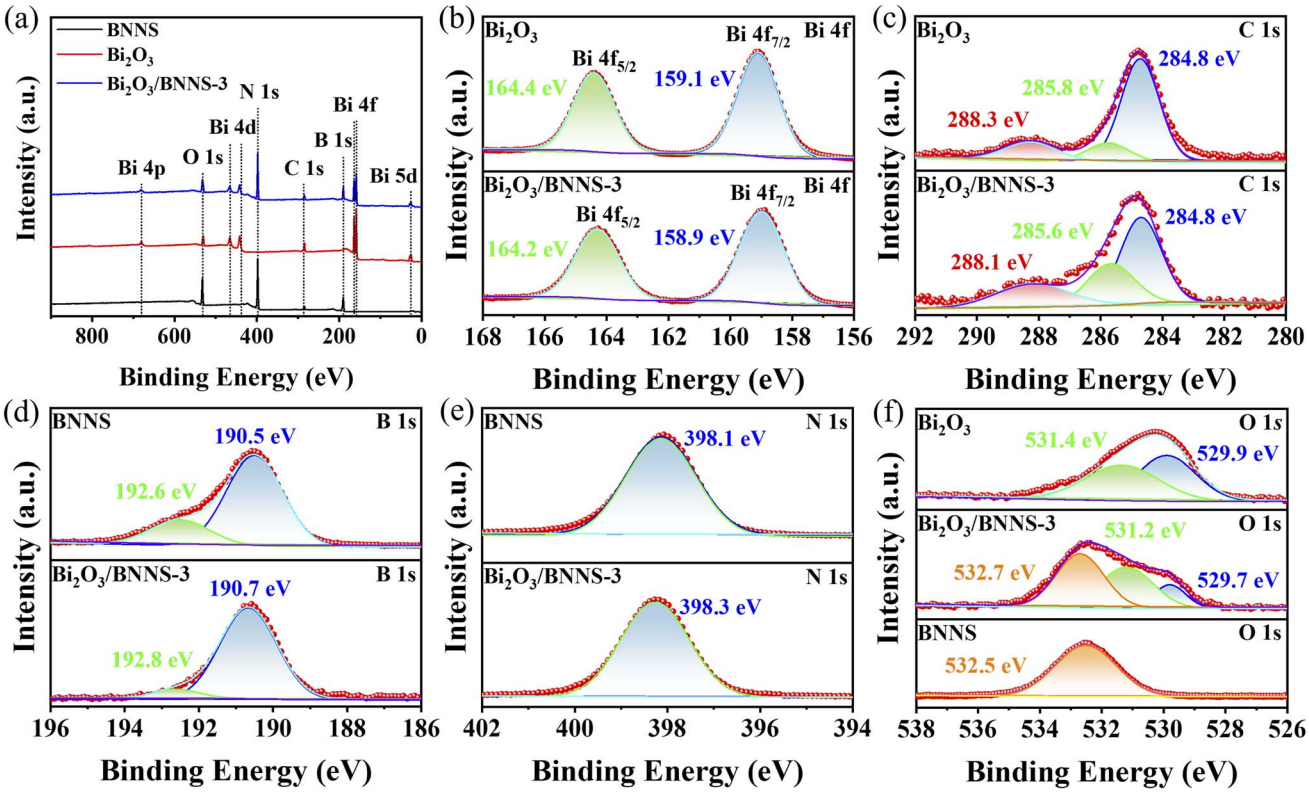

Fig. 2 (a) XPS full spectrum, (b) Bi 4f, (c) C 1s, (d) B 1s, (e) N 1s and (f) O 1s high-resolution XPS spectra of Bi_2O_3, BNNS and Bi_2O_3/BNNS-3.

furnishing an ample number of active sites for the nucleation, growth of Bi_2O_3, and ensuing photocatalytic transformations. The SEM image of the Bi_2O_3/BNNS shows a structure similar to that of BNNS, but upon closer observation, a layer of fine "fuzz" can be seen on its surface. The TEM image (Fig. 3f) showcases a uniform dispersion of nanowires on the surface of BNNS in a more intuitive manner. The HRTEM image (Fig. 3g) intuitively displays the crystal structures of different regions of the composite. Clear lattice fringes are observed in both the sheet-like BNNS and the nanowire structures, with spacings of 3.47 Å and 3.18 Å, corresponding to the (002) plane of h-BN and the (201) plane of β-Bi_2O_3, respectively, confirming that the nanowires are composed of Bi_2O_3. Notably, the two components are in intimate contact, forming a well-defined heterointerface at the junction between BNNS and Bi_2O_3, which confirms the successful construction of the heterojunction. Furthermore, the results indicate that BNNS acts as a growth substrate, effectively regulating the morphology of the Bi_2O_3 nanowires and resulting in a significant reduction in both their diameter and length. Fig. 3h–m exhibit the HAADF and element mapping images of Bi_2O_3/BNNS, providing further evidence of the homogeneous distribution of Bi_2O_3 nanowires on the BNNS surface.

The surface properties of catalysts are one of the main factors affecting the photocatalytic activity. The N_2 adsorption–desorption isotherms of Bi_2O_3, BNNS, and Bi_2O_3/BNNS-3 were examined, with results presented in Fig. 4a. Bi_2O_3 displayed a Type IV isotherm with an H_3 hysteresis loop, indicative of its mesoporous nature. Conversely, BNNS demonstrated a Type I isotherm with an H_4 hysteresis loop, highlighting the presence of abundant micropores and slit-like mesopores resulting from layer-by-layer stacking.[35] In contrast to the aforementioned materials, the Bi_2O_3/BNNS composite material exhibited a typical Type IV isotherm with an H_4 hysteresis loop, exposing its hierarchical porous structure. Fig. 4b illustrates that Bi_2O_3/BNNS-3 displays a narrow pore size distribution centered at 4 nm within the range of 2–8 nm and includes numerous pores with diameters ranging from 8–80 nm. Utilizing the BET method revealed that the cumulative pore volume of Bi_2O_3/BNNS-3 (0.404 $cm^3\ g^{-1}$) exceeded that of BNNS (0.175 $cm^3\ g^{-1}$) and Bi_2O_3 (0.231 $cm^3\ g^{-1}$) (Fig. 4c and d). Furthermore, the specific surface area of Bi_2O_3/BNNS-3 (202.586 $m^2\ g^{-1}$) approximates that of BNNS (225.889 $m^2\ g^{-1}$) but surpasses that of Bi_2O_3 (58.162 $m^2\ g^{-1}$) notably (Fig. 4d). The results suggest that the even dispersion of Bi_2O_3 nanowires on BNNS surface leads to the formation of additional accumulated pores while preserving the pore features of both BNNS and Bi_2O_3. In conclusion, the high pore volume and large specific surface area of composites increase adsorption and reactive sites, enhancing the efficiency of photocatalytic reactions.

The UV-visible absorption spectra of BNNS, Bi_2O_3, and Bi_2O_3/BNNS were analyzed to assess the optical utilization efficiency. As depicted in Fig. 5a, Bi_2O_3 demonstrates outstanding visible light absorption capacity with an absorption edge around 550 nm, whereas BNNS exhibits minimal light absorption within the visible spectrum. Nevertheless, the optical absorption properties of both materials significantly improve across

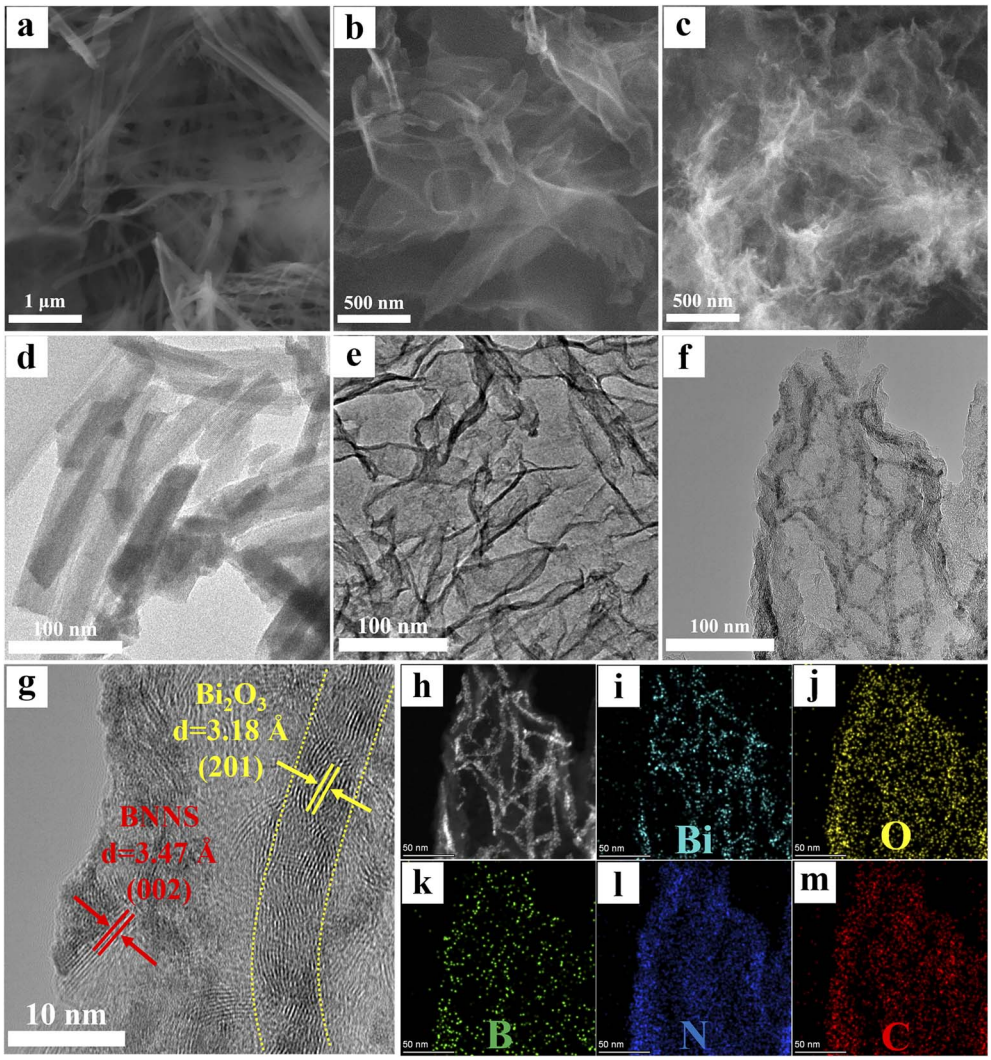

Fig. 3 (a) SEM and (d) TEM images of Bi_2O_3; (b) SEM and (e) TEM images of BNNS; (c) SEM, (f) TEM, (g) HRTEM, (h) HAADF and (i–m) elements mapping images of Bi_2O_3/BNNS composites.

the entire spectrum upon their combination. This enhancement can be attributed to the unique microstructure of the Bi_2O_3/BNNS, which promotes internal light reflection. Based on the provided test data, the band gaps of Bi_2O_3, BNNS and Bi_2O_3/BNNS-3 were determined as 2.32 eV, 3.36 eV and 2.36 eV, respectively, through the application of the Kubelka–Munk formula (refer to Fig. 5b). The presence of various additional elements such as C, O and H elements in the raw materials (H_3BO_3 and $CO(NH_2)_2$) utilized during the synthesis of BNNS, alongside B and N elements, lead to the incorporation of trace impurities within BNNS. This phenomenon can potentially influence the energy level configuration of h-BN as reported in the literature, consequently resulting in a narrower band gap for BNNS compared to the typical range observed in h-BN (5–6 eV).

Analyzing the band structures of Bi_2O_3 and BNNS enhances the understanding of the transfer mechanisms involved with photogenerated carriers in Bi_2O_3/BNNS. The Mott–Schottky plots of Bi_2O_3 and BNNS (Fig. 5c and d) demonstrate that the negative slope of the Bi_2O_3 curve confirms its classification as a p-type semiconductor, consistent with previously reported findings, while the positive slope of the BNNS plot indicates its n-type semiconductor characteristics.[36] Calculations reveal that the flat band potentials (E_{fb}) for Bi_2O_3 and BNNS are 0.55 V and −0.97 V, respectively, relative to the Ag/AgCl electrode. Given that the flat band potential of a p-type semiconductor approximates its valence band maximum (E_{VB}), and that of an n-type semiconductor approximates its conduction band minimum (E_{CB}), and using the previously determined band gaps of Bi_2O_3 and BNNS (2.32 eV and 3.36 eV, respectively), the E_{VB} and E_{CB} of Bi_2O_3 are calculated to be 0.75 V and −1.57 V (*vs.* NHE), while the E_{CB} and E_{VB} of BNNS are −0.77 V and 2.59 V (*vs.* NHE), respectively.

To validate the accuracy of the aforementioned results, the VB-XPB spectra of Bi_2O_3 and BNNS were tested and analyzed. The findings are illustrated in Fig. 6e and f, while the calculation formulas for $E_{VB,\ NHE}$ are presented in eqn (2):

$$E_{VB,\ NHE} = \varphi + E_{VB,\ XPS} - 4.44 \quad (1)$$

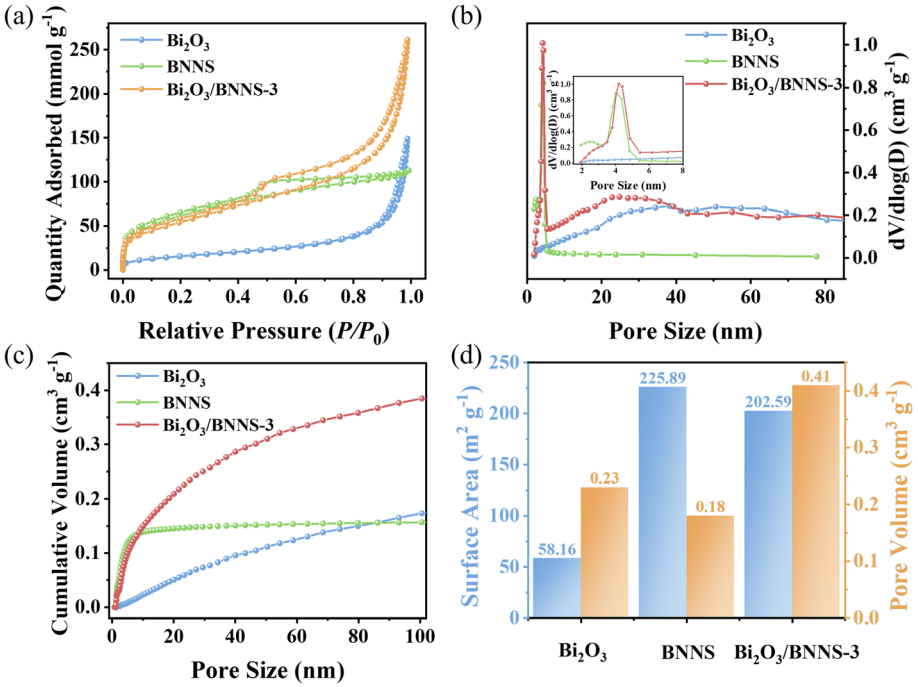

Fig. 4 (a) N_2 adsorption–desorption isotherms, (b) pore size distribution curves, (c) cumulative pore volume curves and (d) specific surface area/cumulative pore volume plots for Bi_2O_3, BNNS and Bi_2O_3/BNNS-3.

The power function used in VB-XPS testing, denoted as φ (4.60 eV),[37] facilitates the calculation of the $E_{VB,\ NHE}$ values for Bi_2O_3 and BNNS, which are 0.75 eV and 2.59 eV, respectively. Furthermore, the $E_{CB,\ NHE}$ values are −1.57 eV and −0.77 eV, respectively. These results align with those obtained from Mott–Schottky curve calculations, leading to the conclusion that the

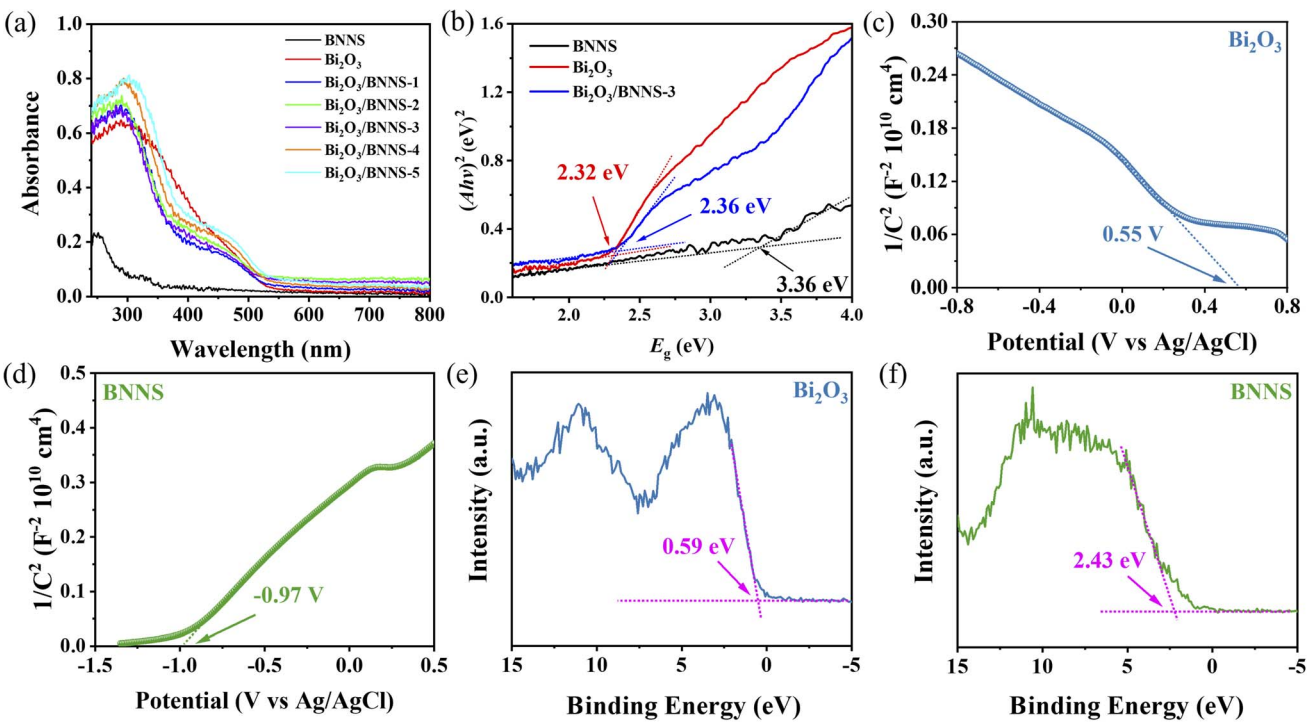

Fig. 5 (a) UV-vis absorption spectra of BNNS, Bi_2O_3 and Bi_2O_3/BNNS composites; (b) bandgap of BNNS, Bi_2O_3 and Bi_2O_3/BNNS-3; (c and d) Mott–Schottky curves and (e and f) VB-XPS spectra of Bi_2O_3 and BNNS.

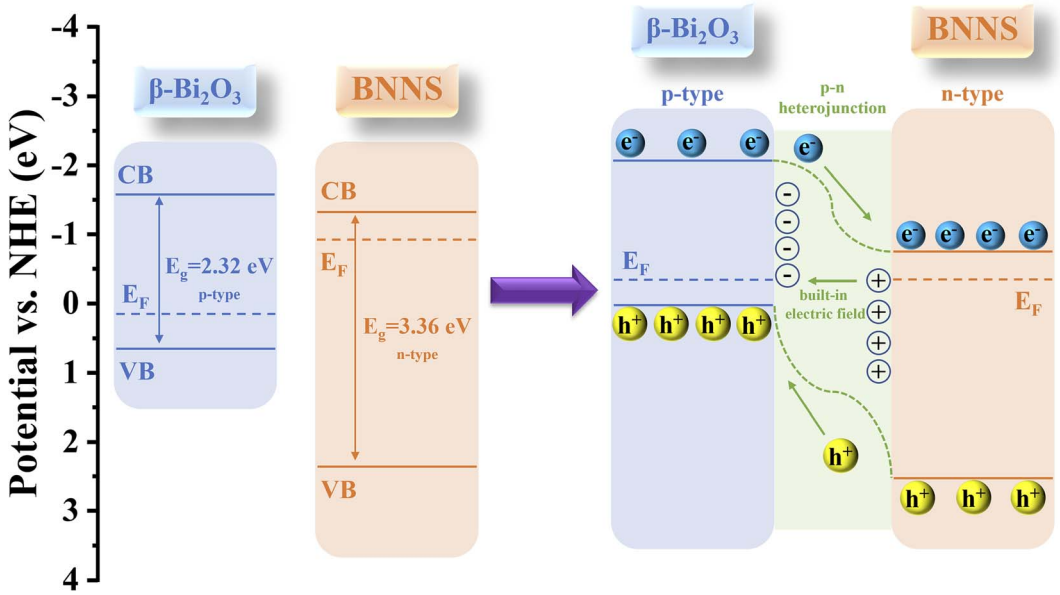

Fig. 6 Schematic diagram of the energy band structures of Bi_2O_3, BNNS and Bi_2O_3/BNNS.

energy band structures of Bi_2O_3 and BNNS are represented in Fig. 6 (left). As a p–n junction forms between Bi_2O_3 and BNNS, their Fermi levels (E_F) gradually align, prompting the energy bands of Bi_2O_3 and BNNS to shift downward and upward, respectively. As a result (as illustrated in Fig. 6 right), in the dark equilibrium state, the depletion of electrons in n-type BNNS induces a positive space charge at BNNS, while the depletion of holes in p-type Bi_2O_3 induces a negative space charge at Bi_2O_3, thereby establishing a built-in electric field directed from BNNS to Bi_2O_3. Under illumination, driven by this built-in electric field, photogenerated electrons transfer from Bi_2O_3 to BNNS and photogenerated holes transfer from BNNS to Bi_2O_3, suppressing the recombination of photogenerated carriers.

The separation efficiency of photogenerated charge carriers significantly impacts the photocatalytic performance of catalysts. The recombination kinetics of photo-induced charge carriers in Bi_2O_3 and Bi_2O_3/BNNS were analyzed using time-resolved photoluminescence spectroscopy (TRPL). As shown in Fig. 7a, fitting the experimental data with a double exponential fitting model the charge carrier lifetimes in the composite materials were all extended compared to Bi_2O_3 (18.63 ns), particularly for Bi_2O_3/BNNS-3 (21.73 ns). This phenomenon demonstrates that the presence of p–n junctions greatly improves the separation and transport of photogenerated charge carriers in the catalyst. The electrochemical behavior of semiconductor materials can provide insights into the charge carrier separation efficiency. Fig. 7b exhibits the photocurrent responses of BNNS, Bi_2O_3, and Bi_2O_3/BNNS composites showing that all materials exhibit current generation under illumination, with the composite materials showing higher photocurrent density than BNNS and Bi_2O_3. In addition, the electrochemical impedance spectroscopy (EIS) curves of semiconductor materials can be used to study the resistance encountered during the charge transfer process. The results (Fig. 7c) show that the EIS impedance of the composite materials is lower than that of BNNS and Bi_2O_3. In conclusion, the

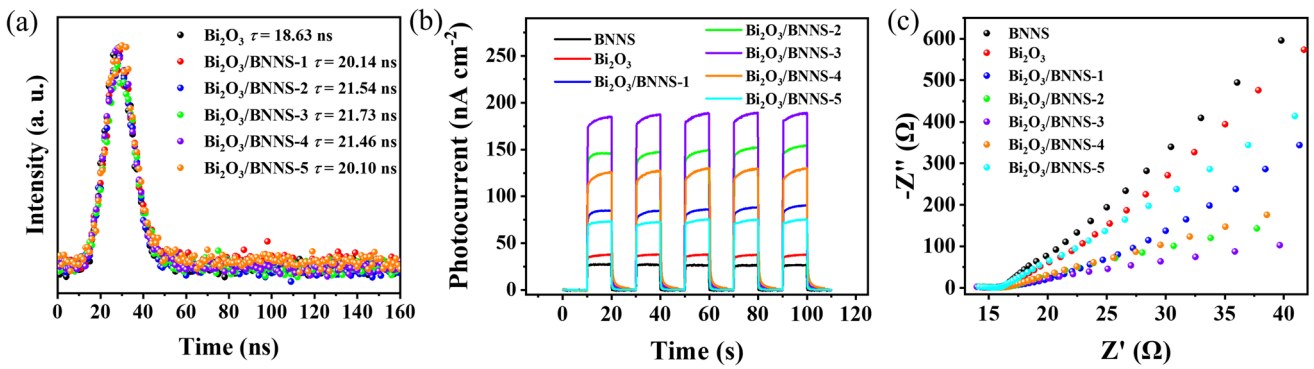

Fig. 7 (a) The TRPL spectra of Bi_2O_3 and Bi_2O_3/BNNS composites; (b) the transient photocurrent curve and (c) electrochemical impedance curves of BNNS, Bi_2O_3 and Bi_2O_3/BNNS composites.

photoelectrochemical data further confirm that the existence of internal p–n junctions and built-in electric fields in Bi_2O_3/BNNS composites facilitate the establishment of effective charge transfer routes, resulting in superior charge carrier separation rates and efficient charge transfer.

The TC solution with a concentration of 50 mg L^{-1} and a 300 W xenon lamp (λ = 300–420 nm) were employed as the simulated contaminant and the light source, respectively, to evaluate the photocatalytic activity of BNNS, Bi_2O_3, and Bi_2O_3/BNNS composites for TC removal. As shown in Fig. 8a, a 60-minute dark adsorption step was first performed. The results confirm that 60 min is sufficient to reach adsorption equilibrium, ensuring that the subsequent concentration decrease under light irradiation is attributed solely to photocatalytic degradation. During the dark adsorption period, BNNS and Bi_2O_3/BNNS composites exhibited notably higher adsorption capacity for TC compared to Bi_2O_3. Furthermore, Fig. 8a illustrates that after 120 min of photocatalytic reaction, BNNS and Bi_2O_3 achieved removal rates of 58.43% and 38.62% for TC, respectively. The composites demonstrated removal rates above 80% under the same conditions, with Bi_2O_3/BNNS-3 exhibiting the highest efficiency at 94.65%. The results show relatively small error ranges (<5%), indicating that the experimental data possess good reproducibility and reliability.[38] These results indicate that the superior performance of Bi_2O_3/BNNS-3 is not driven solely by BNNS adsorption, but rather originates from the synergistic effect between adsorption and photocatalysis. It is noteworthy that BNNS exhibits semiconductor characteristics, which suggest its potential for photocatalytic degradation.

To assess the photocatalytic degradation rates of TC molecules, the first 80 minutes, during which the reaction rate is relatively high, was chosen as the evaluation time interval, employing the pseudo-first-order kinetic model for BNNS, Bi_2O_3, and Bi_2O_3/BNNS composites. Fig. 8b and c illustrate that the photocatalytic degradation processes of TC molecules for all materials adhere to the pseudo-first-order kinetic model. The calculated kinetic constants (K) for BNNS and Bi_2O_3 are 0.285 × 10^{-2} and 0.372 × 10^{-2} min^{-1}, respectively. The kinetic constants of Bi_2O_3/BNNS composites are higher than BNNS and Bi_2O_3 due to the formation of a p–n junction. Specifically, the kinetic constant of Bi_2O_3/BNNS-3 is the highest at 2.177 × 10^{-2} min^{-1}. The photocatalytic activity of BNNS is weak, therefore, with the further increase of BNNS content, the kinetic constants of the composites decrease, indicating a decline in photocatalytic activity.

To further explore the active species involved in the photocatalytic degradation of Bi_2O_3/BNNS composites, particularly Bi_2O_3/BNNS-3, a set of radical trapping experiments were conducted. PBQ, TEOA and IPA were utilized to capture the $\cdot O_2^-$, h^+ and ·OH within the system. In Fig. 8d, it is evident that the introduction of TEOA had a negligible impact on the photocatalytic degradation of TC. Conversely, the presence of PBQ and IPA led to varying degrees of suppression in the TC degradation process, with suppression efficiencies of 54.21% and 39.76%, respectively. Therefore, the $\cdot O_2^-$ and ·OH contribute to the photocatalytic degradation of TC in the Bi_2O_3/BNNS composites system, with $\cdot O_2^-$ playing a crucial role. To further validate the involvement of these radicals, ESR spin-trapping

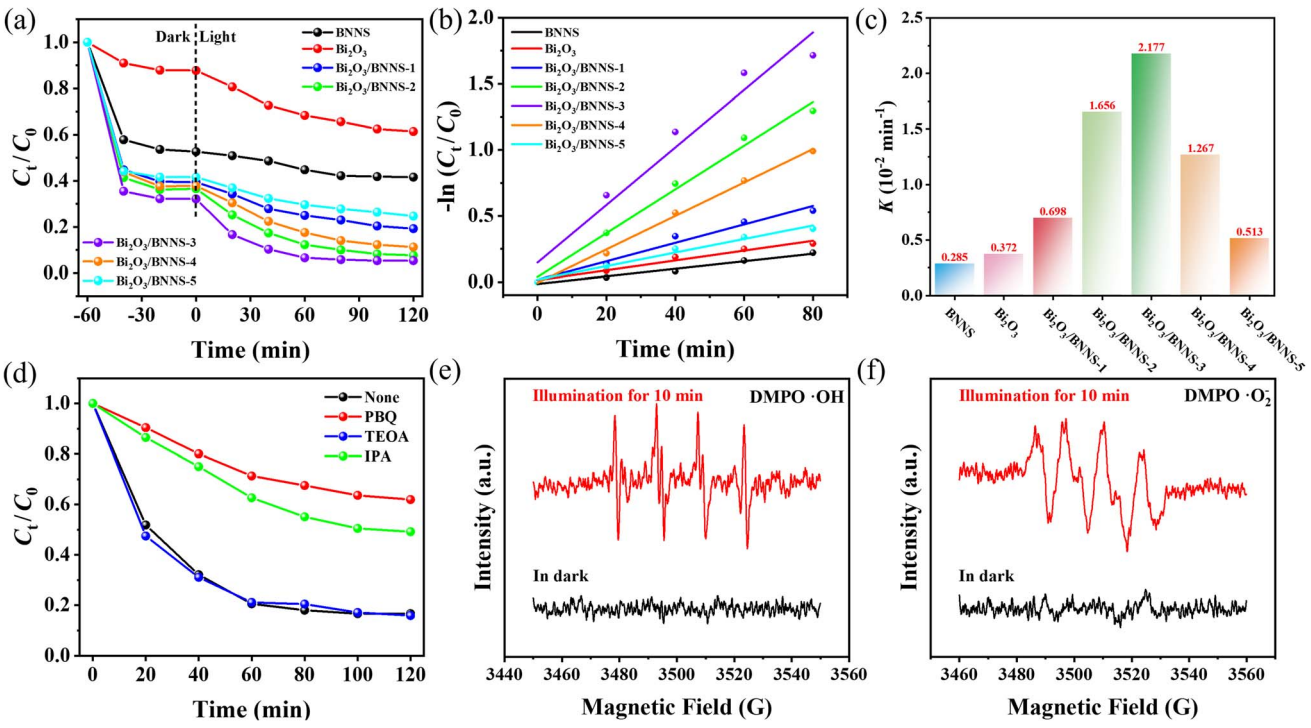

Fig. 8 (a) Photocatalytic degradation curves, (b) first level kinetic model fitting and (c) rate constants of BNNS, Bi_2O_3 and Bi_2O_3/BNNS composites for tetracycline; (d) the photocatalytic degradation of TC curves by Bi_2O_3/BNNS-3 after adding different trapping agents, respectively; ESR signals of (e) DMPO-·OH and (f) DMPO-$\cdot O_2^-$.

experiments were carried out. As shown in Fig. 8e and f, characteristic signals of DMPO-·OH and DMPO-·O_2^- were clearly observed under illumination, respectively, directly confirming the generation of hydroxyl radicals and superoxide radicals in the photocatalytic system. This outcome is consistent with the radical trapping results, further corroborating that ·OH and ·O_2^- are the main reactive oxygen species responsible for TC degradation.

Considering the cost of photocatalysts in practical applications is mainly dependent on the recycling ability of the material, this work conducted a further assessment of the photocatalytic degradation efficiency of TC using the Bi_2O_3/BNNS composites after four cycles of reuse. The detailed experimental procedure was as follows: after each photocatalytic reaction, the used Bi_2O_3/BNNS composite was collected by centrifugation, washed alternately with deionized water and absolute ethanol, dried, and then calcined at 150 °C for 2 h before being used in the next cycle. The findings from Fig. 9a illustrated that following four cycles, the photocatalytic degradation efficiency of Bi_2O_3/BNNS-3 remained at 93.64% of the initial value, demonstrating good reusability of the composite. Subsequently, the photocatalyst after four cycles was analyzed by XRD and FT-IR, comparing the data with the pre-cycling measurements. To evaluate the structural stability and assess the potential photocorrosion of Bi_2O_3, as depicted in Fig. 9b, there were insignificant alterations in the crystalline structure and phase composition of Bi_2O_3/BNNS-3 pre and post-reaction; no attenuation or emergence of new impurity peaks for the characteristic diffraction peaks of Bi_2O_3 was observed. A slight increase in crystallinity was observed after the reaction, likely attributed to the hydrolysis of certain unstable structures. This indicates that under the experimental conditions, no obvious photocorrosion of Bi_2O_3 occurred in the Bi_2O_3/BNNS composite, which can be attributed to the p–n heterojunction that facilitates electron transfer from BNNS to Bi_2O_3, effectively reducing hole accumulation on the Bi_2O_3 surface. Additionally, results from the FT-IR analysis (Fig. 9c) disclosed an augmentation in the intensity of O–H and C–H bonds in Bi_2O_3/BNNS-3 post-cycling, indicating the adsorption of a minor quantity of TC molecules or other degradation by-products on the catalyst surface. Nevertheless, the chemical structure and composition of the catalyst itself remained unaltered. Hence, the Bi_2O_3/BNNS composites exhibit remarkable structural stability and reusability.

Using Bi_2O_3/BNNS-3 as a model, UV-vis spectra of the TC solution were analyzed during the degradation process. As illustrated in Fig. 10a, following 60 minutes of adsorption, a significant decrease in the UV-vis spectral intensity of the solution was observed. Subsequently, post-photocatalytic degradation, the UV-vis absorption spectrum of the solution exhibited substantial deviations from that of the TC solution, indicating the decomposition of TC molecules into other compounds. TC molecules, characterized by numerous double bonds, amino groups, aromatic rings, and phenolic structures, are prone to reactive free radical attacks.[39] Employing liquid chromatography-mass spectrometry allows for the examination and analysis of intermediate components in the photocatalytic degradation process, facilitating a comprehensive investigation into the degradation mechanism of TC molecules. Fig. 10b illustrates the presence of a substantial number of intermediates in the liquid phase following 20 minutes of photocatalytic degradation. Fig. 10c presents the liquid-phase mass spectrometry images of the TC solution and the solution after 120 minutes of degradation. A comparative analysis reveals that the peak corresponding to the TC molecule ($m/z = 445$) has entirely vanished post-degradation, suggesting that the TC molecule has undergone oxidation and reduction to form various other substances through the action of active species. Finally, based on these experimental results, three potential degradation pathways for TC molecules are proposed in Fig. 10d. Pathway I initiates with the deamination of the TC molecule ($m/z = 445$), leading to the formation of T1 ($m/z = 385$) subsequent to ·OH radical attack. T1 then progresses into T2 ($m/z = 341$) and successively evolves into T3 ($m/z = 290$) and T4 ($m/z = 246$) through a sequence of ring-opening and molecular oxidation processes.[40] In Pathway II, the interaction of the TC molecule with h^+ and ·O_2^- radicals triggers a cascade of dealkylation, ring-opening, and dealkylation reactions resulting in the production of T5 ($m/z = 353$), T6 ($m/z = 274$), and T7 ($m/z = 230$).[41] In Pathway III, the relatively low N–C bond energy

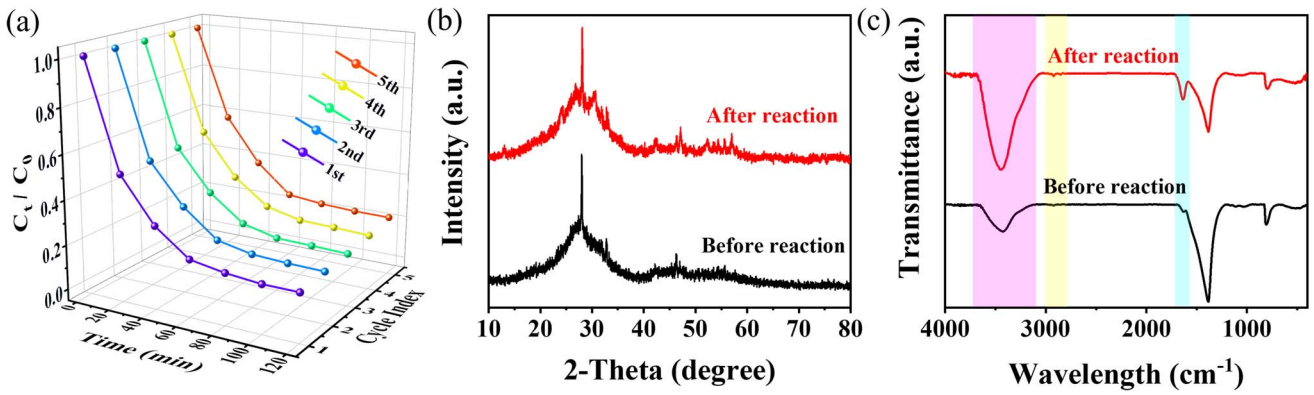

Fig. 9 (a) Five cycles degradation curve of Bi_2O_3/BNNS-3 on TC solution; (b) XRD and (c) FT-IR patterns of Bi_2O_3/BNNS-3 before and after cycling.

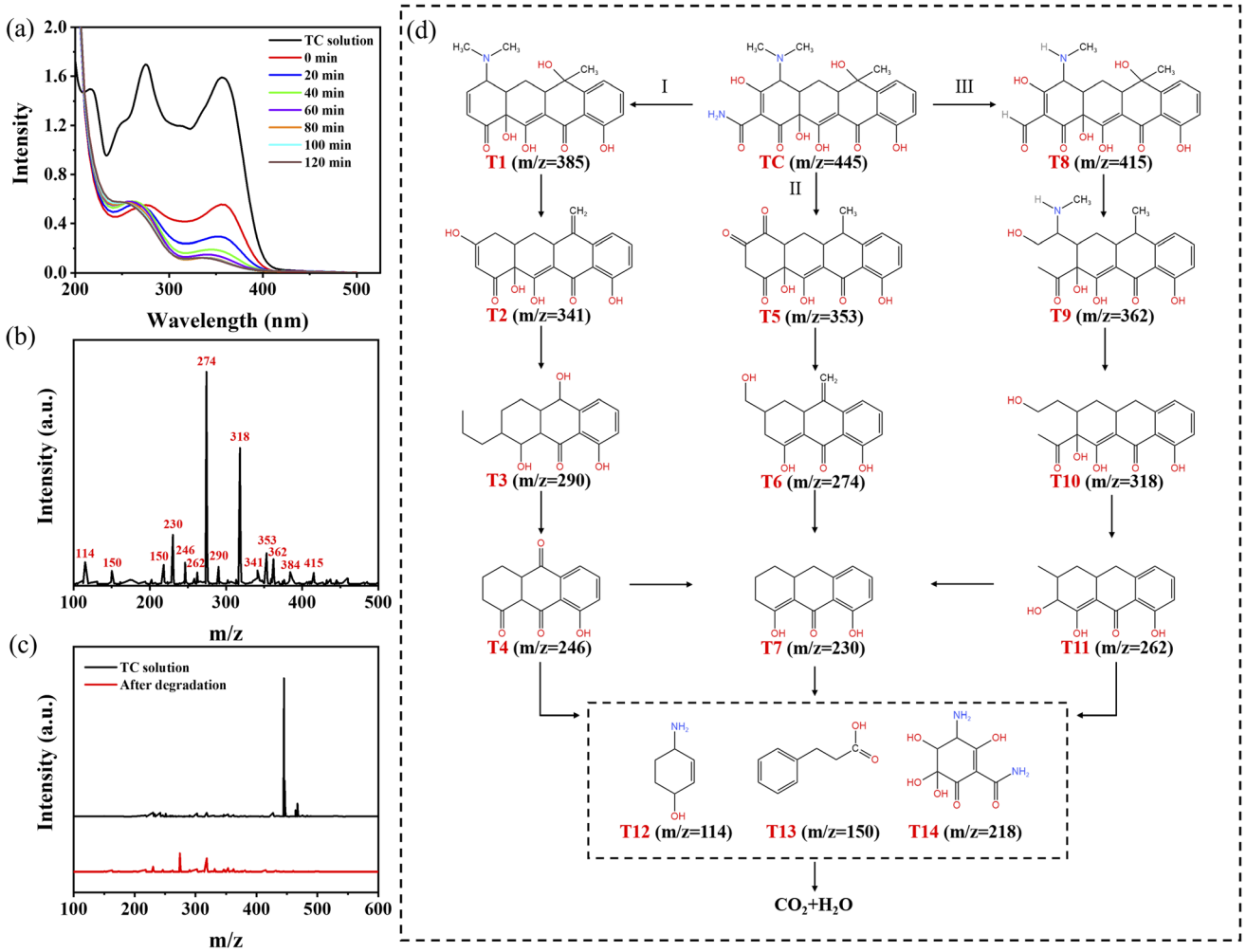

Fig. 10 (a) UV-vis absorption spectra of TC solution during photocatalytic degradation; (b) liquid-phase mass spectra of the solution under light for 20 min, (c) liquid-phase mass spectra of the TC solution and the solution under light for 120 min and (d) presumed photocatalytic degradation process.

facilitates deamination and dealkylation of the TC molecule under the influence of $\cdot O_2^-$ and $\cdot OH$ radicals, yielding T8 (m/z = 417). Following dehydration into an intermediate T9 (m/z = 362), it further undergoes dealkylation and ring-opening processes catalyzed by radicals to generate T10 (m/z = 318) and T11 (m/z = 262).[42] As the photocatalytic oxidation progressed, the aforementioned intermediates were further transformed into lower molecular weight compounds, such as T12 (m/z = 114), T13 (m/z = 150), and T14 (m/z = 218),[43] and were ultimately mineralized into water and carbon dioxide.

Industrial wastewater typically contains a diverse array of complex components, whereas the TC solution utilized in our experiments is characterized by high purity and the absence of extraneous substances. To better simulate real wastewater conditions and evaluate the practical applicability of the Bi_2O_3/BNNS-3, we conducted photocatalytic degradation experiments in the presence of typical groundwater ions at environmentally relevant concentrations: bicarbonate (100 mg L^{-1} as HCO_3^-), sulfate (50 mg L^{-1}), chloride (50 mg L^{-1}), calcium (50 mg L^{-1}), and magnesium (20 mg L^{-1}).[44–46] The degradation efficiencies of tetracycline under different ion conditions are shown in Fig. 11a, which were as follows: bicarbonate (86.3%), chloride (83.7%), calcium (79.2%), sulfate (72.5%), and magnesium (70.7%). Bicarbonate and chloride exhibited relatively minor inhibitory effects on degradation efficiency, with removal rates remaining above 80%. In contrast, calcium, sulfate, and magnesium showed more pronounced suppression, which may be attributed to competitive adsorption between anions (particularly sulfate) and tetracycline molecules for the limited active sites on the catalyst surface, as well as the ion shielding effect induced by cations (calcium and magnesium). Despite the inhibitory effects of these coexisting ions, the Bi_2O_3/BNNS composite maintained a tetracycline removal rate of over 70% under all tested conditions, demonstrating its robust photocatalytic degradation capability and potential for real-world wastewater treatment applications. Furthermore, Bi_2O_3/BNNS-3 exhibits excellent photocatalytic degradation capabilities for both oxytetracycline (OTC) and doxycycline (DC) as shown in Fig. 11b. In conclusion, Bi_2O_3/BNNS composites possess

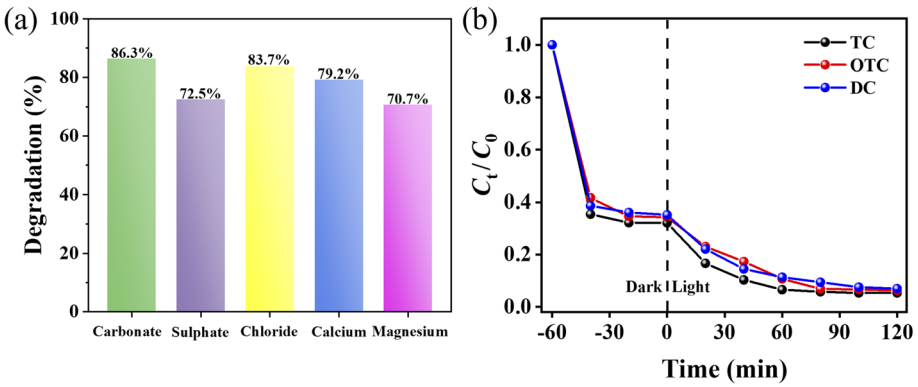

Fig. 11 (a) TC degradation curves of Bi_2O_3/BNNS-3 in inorganic salt ion coexistence environment; (b) degradation curves of Bi_2O_3/BNNS-3 on TC, OTC and DC.

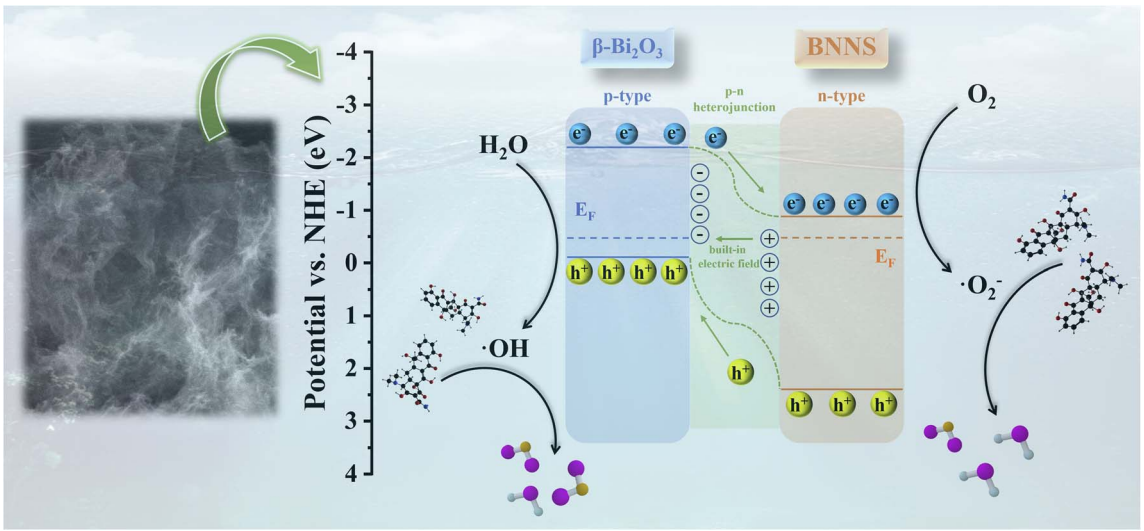

Fig. 12 Photocatalytic degradation mechanism of TC by Bi_2O_3/BNNS composites.

significant photocatalytic degradation potential for practical applications.

Based on the previous discussion, the proposed mechanism for the photocatalytic degradation of tetracycline (TC) molecules using the Bi_2O_3/BNNS composites is illustrated in Fig. 12. In the composites, the p-type semiconductor Bi_2O_3 and the n-type semiconductor BNNS form a p–n junction. Due to the alignment of their Fermi levels, the band structures of both materials experience shifts, resulting in a more positive valence band and a more negative conduction band for the composite compared to each component. This alteration enhances the oxidation–reduction capabilities of the photogenerated electrons and holes. Under illumination, the photogenerated charge carriers in the two materials migrate due to the influence of the p–n junction: electrons generated in Bi_2O_3 transfer to the surface of BNNS, while holes produced in BNNS move to the surface of Bi_2O_3. This migration not only inhibits the recombination of photogenerated charge carriers but also establishes an internal built-in electric field within the catalyst, thereby facilitating an increased rate of charge carrier transfer. Moreover, the accumulation of photogenerated electrons and holes at the surfaces of BNNS and Bi_2O_3, respectively, results in the generation of superoxide radicals ($·O_2^-$) and hydroxyl radicals (·OH) on their surfaces. These free radicals subsequently engage in redox reactions with TC molecules, ultimately leading to their degradation into water, carbon dioxide, and other small molecular byproducts.

4. Conclusion

In this study, a solvent-thermal method was employed to fabricate high-performance Bi_2O_3/BNNS composites with synergistic adsorption–photocatalysis capabilities. The experimental results reveal that BNNS, serving as the growth substrate for Bi_2O_3 nanowires, effectively controls the growth and aggregation, resulting in enhanced specific surface area, pore volume, and robust adsorption capacity of the composites. Additionally, BNNS demonstrates n-type semiconductor properties, and the formation of a p–n junction and built-in electric field between Bi_2O_3 and BNNS promotes efficient separation of

photogenerated electrons and holes within the catalyst, leading to superior photocatalytic activity of the composite material. Notably, both the adsorption capacity and photocatalytic degradation efficiency of the composite material outperform those of Bi_2O_3 and BNNS individually. Furthermore, the optimized concentration of Bi_2O_3/BNNS-3 at 50 mg L^{-1} achieves degradation rates exceeding 90% for TC, OTC, and DC solutions, with degradation performance unaffected by various impurity ions. Additional validation through free radical capture experiments, UV-vis spectroscopy, and liquid-phase mass spectrometry confirms that under simulated sunlight, the Bi_2O_3/BNNS composite material facilitates the oxidation of TC molecules into CO_2, H_2O, and other smaller compounds through the generation of $\cdot OH$ and $\cdot O_2^-$. Overall, this research underscores the substantial potential of Bi_2O_3/BNNS composites in the photocatalytic degradation of water pollutants.

Author contributions

Zhao Du: conceptualization, writing – original draft, writing – review & editing, investigation; Yanan Wu: visualization; Mengmeng Yu: formal analysis; Zishuang Cheng: project administration; Po Hu: validation verification; Zhonglu Guo: formal analysis; Chengchun Tang: project administration, resources; Guifeng Chen: supervision, project administration; Yi Fang: supervision, project administration.

Conflicts of interest

There are no conflicts to declare.

Data availability

Data can be accessed upon reasonable request from the corresponding author at hebutdz@163.com.

Acknowledgements

This work was supported by Youth Fund of Natural Science Foundation of Henan Province (252300423430), the project for Science and Technology Correspondent of Tianjin City (No. 20YDTPJC01710) and S&T Program of Hebei (199676242H).

References

1 Z. Xia, L. Wang, W. Tan, L. Yuan, T. Shen, Y. Liu and Z. Jiao, Construction of dual Z-scheme UiO-66-NH_2/BiOCl/BiOI heterojunction for synergistic photocatalytic CO_2 reduction and organic pollutant degradation, *J. Colloid Interface Sci.*, 2025, **699**, 138184.

2 Y. Jin, T. Wang, T. Zhan, N. Ma and W. Dai, Interface-electronically engineered MOF-on-MOF heterojunctions exhibiting dual light-driven functions: Synergistic fluorescence diagnosis and photocatalytic remediation of antibiotic contamination, *J. Mol. Struct.*, 2025, **1346**, 143183.

3 L. Shi, G. Wang, K. Tang, C. Yang, J. Yang, S. Xiong, A. Tang and X. Zhang, Montmorillonite improved the tetracycline degradation performance of Br-doped BiOCl photocatalyst, *Chem. Eng. Sci.*, 2025, **318**, 122188.

4 M. Ding, M. Li, Z. Li, J. Nie, X. Lyu and Z. Jin, Construction of magnetic recoverable $CoFe_2O_4$/$Mn_{0.5}Cd_{0.5S}$ heterojunction for photocatalytic hydrogen evolution and tetracycline degradation, *Appl. Surf. Sci.*, 2025, **710**, 164041.

5 F. Feng, X. Zhang, X. Xu, Q. Huang, H. Yin, R. Li, G. Wu and W. Xing, Construction of 2D/3D biochar modified g-C_3N_4 for efficient removal of tetracycline hydrochloride via photocatalytic PMS activation, *Opt. Mater.*, 2025, **167**, 117246.

6 L. Nie, K. Wang, W. Zhao, C. Zhang and T. Shen, Enhanced performance of hierarchical porous HKUST-1/g-C_3N_4 heterostructure in the degradation of antibiotics with and without light, *Sep. Purif. Technol.*, 2025, **376**, 133894.

7 M. Rizwan, K. Kayani, Z. Qamar, Z. Liu and V. A. L. Roy, Cobalt ferrite-MXene nanohybrid: A dual-action approach for synergistic doxorubicin removal through adsorption-photocatalysis, *Sep. Purif. Technol.*, 2025, **372**, 133405.

8 M. Pan, R. Gao, S. Liang, X. Hu, M. Xie, W. Chen and S. Wang, Oxygen vacancies-rich bimetallic Zr/Co-UiO-66 materials for bifunctional adsorption-photodegradation of tetracycline antibiotics in water, *Chem. Eng. J.*, 2025, **517**, 164397.

9 J. Suo, Y. Dai, L. Yin and Q. Hua, Stable cobalt-doped MOF/PAN electrospun membrane: Enhanced tetracycline degradation via adsorption and dual free radical pathways, *Chem. Eng. J.*, 2025, **519**, 164956.

10 S. Wang, Y. Li, Z. Li, L. Xu, Z. Yin, J. Qiu, Z. Yang and Z. Song, Amorphous/crystalline interface of Bi/Bi_4NbO_8Cl heterostructure for improved piezo-photocatalysis, *Small*, 2025, **21**, 2500758.

11 P. Lu, Y. Peng, Y. Yang, S. Chen, J. Shang, C. Yang, M. Xu, J. Bai, Z. Zhao and X. Hu, Visible-light-driven photocatalytic for degrading tetracycline wastewater by BiOI/Bi_2O_3 Z-scheme heterojunction, *J. Environ. Chem. Eng.*, 2024, **12**, 114395.

12 W. Dou, X. Hu, L. Kong and X. Peng, Photo-induced dissolution of Bi_2O_3 during photocatalysis reactions: Mechanisms and inhibition method, *J. Hazard. Mater.*, 2021, **412**, 125267.

13 H. Li, X. Luo, Z. Long, G. Huang and L. Zhu, Plasmonic Ag nanoparticle-loaded n-p $Bi_2O_2CO_3$/α-Bi_2O_3 heterojunction microtubes with enhanced visible-light-driven photocatalytic activity, *Nanomaterials*, 2022, **12**, 1608.

14 M. T. Ayala-Ayala, A. I. Gutiérrez Pérez, P. S. Cardenas Terrazas, J. González-Hernández, D. W. Bahnemann and J. Muñoz-Saldaña, Nanostructured β-Bi_2O_3/Cu_2O heterojunctions synthesized via mechanical milling for visible-light region photocatalysis, *ACS Appl. Nano Mater.*, 2025, **8**, 8663–8675.

15 L. Peng, W. Lou, L. Li, Y. Zhang, X. Luo, N. Xu and J. Qiao, Boosting the electrochemical CO_2 reduction performance by Cu_2O/β-Bi_2O_3 bimetallic heterojunction with the assistance of light, *Sep. Purif. Technol.*, 2024, **330**, 125372.

16 T. Wang, Q. Zhu, C. Huo, Z. Yin, Q. Shi, J. Tao, F. Su and S. Cao, Constructing flower-like TiO_2/Bi_2O_3 p–n

heterojunction with enhanced visible-light photocatalytic performance, *J. Alloys Compd.*, 2023, **950**, 169889.

17 Z. Tan, C. Shi, Z. Shi, H. Yang, J. yang, C. Wu and D. Wang, Synthesis of nano-silver decorated β-Bi_2O_3/$Bi_2O_2CO_3$ heterojunction using Bi-MOF precursor: Precisely controllable structure and enhanced photocatalytic activity for sulfadiazine degradation, *J. Alloys Compd.*, 2024, **1005**, 176049.

18 S. Yang, F. Zhang, Y. Shang, L. Luo and Z. Liu, Highly efficient photocatalytic degradation of refractory organic pollutants onto designed boron nitride: Morphology control and oxygen doping, *J. Cleaner Prod.*, 2023, **429**, 139532.

19 G. Vijay, S. S. Dhavud, S.-M. Chen, Z. M. Riyas, M. Sethupathi, K. R. Ramalingam and M. Sivakami, Two-dimensional hexagonal boron nitride (h-BN) decorated on CeO_2 heterojunction nanocomposite for improved photocatalysis degradation and antibacterial application, *Diamond Relat. Mater.*, 2025, **157**, 112494.

20 C. Zhou, C. Lai, C. Zhang, G. Zeng, D. Huang, M. Cheng, L. Hu, W. Xiong, M. Chen, J. Wang, Y. Yang and L. Jiang, Semiconductor/boron nitride composites: Synthesis, properties, and photocatalysis applications, *Appl. Catal., B*, 2018, **238**, 6–18.

21 Z. Du, L. Feng, Z. Guo, T. Yan, Q. Hu, J. Lin, Y. Huang, C. Tang and Y. Fang, Ultrathin h-BN/Bi_2MoO_6 heterojunction with synergetic effect for visible-light photocatalytic tetracycline degradation, *J. Colloid Interface Sci.*, 2021, **589**, 545–555.

22 D. Liu, W. Lei, S. Qin, K. D. Klika and Y. Chen, Superior adsorption of pharmaceutical molecules by highly porous BN nanosheets, *Phys. Chem. Chem. Phys.*, 2016, **18**, 84–88.

23 J. Li, X. Xiao, X. Xu, J. Lin, Y. Huang, Y. Xue, P. Jin, J. Zou and C. Tang, Activated boron nitride as an effective adsorbent for metal ions and organic pollutants, *Sci. Rep.*, 2013, **3**, 3208.

24 Q. Song, Y. Fang, Z. Liu, L. Li, Y. Wang, J. Liang, Y. Huang, J. Lin, L. Hu, J. Zhang and C. Tang, The performance of porous hexagonal BN in high adsorption capacity towards antibiotics pollutants from aqueous solution, *Chem. Eng. J.*, 2017, **325**, 71–79.

25 Z. Du, H. Cai, Z. Zhao, Z. Guo, J. Lin, Y. Huang, C. Tang, G. Chen and Y. Fang, Facile synthesis of graphene quantum dots and C-doping porous BN nanoribbon heterojunctions for boosting CO_2 photoreduction, *Sep. Purif. Technol.*, 2023, **311**, 123321.

26 J. Zhou, F. Duo, C. Wang, L. Chu, M. Zhang and D. Yan, Robust photocatalytic activity of two-dimensional h-BN/Bi2O3 heterostructure quantum sheets, *RSC Adv.*, 2022, **12**, 13535–13547.

27 N. Xu, Y. Zheng, J. Chen, J. Dai, X. Zhao, J. Ma and R. Liu, Ti-doped synergistic hollow thin-walled Bi_2O_3 nano-microspheres for efficient tetracycline hydrochloride photodegradation, *Colloids Surf., A*, 2024, **701**, 134887.

28 Y. Li, J. Song, X. Zhao, B. Li, Z. Wang, J. Yang, G. Ban, F. Teng, J. Ma, C. Meng, H. Ye, G. Chen, Z. Dai and Y. Cong, Ag nanoparticles supported on h-BN/$BiPO_4$ heterostructures as a photocatalyst for the degradation of Rhodamine B, *ACS Appl. Nano Mater.*, 2024, **7**, 9116–9125.

29 W. Liu, M. Sun, Z. Ding, B. Gao and W. Ding, Ti_3C_2 MXene embellished g-C_3N_4 nanosheets for improving photocatalytic redox capacity, *J. Alloys Compd.*, 2021, **877**, 160223.

30 C. Cao, J. Yang, S. Yang, W. Bai, D. Wang, S. Yan, Y. Xue, X. Qu and C. Tang, Pressureless consolidation of boron nitride fiber ceramics via a chemical bonding approach, *J. Eur. Ceram. Soc.*, 2023, **43**, 5223–5230.

31 X. Qi, X. Xiong, H. Cai, X. Zhang, Q. Ma, H. Tan, X. Guo and H. Lv, Carbon dots-loaded cellulose nanofibrils hydrogel incorporating Bi_2O_3/BiOCOOH for effective adsorption and photocatalytic degradation of lignin, *Carbohydr. Polym.*, 2024, **346**, 122601.

32 S. Liao, M. Arif, X. Qian and G. He, Direct Z-scheme charge transfer Bi_2O_3/UiO-66-NH_2 heterojunctions for boosted photocatalytic degradation of tetracycline hydrochloride in different water systems, *J. Solid State Chem.*, 2024, **336**, 124746.

33 Y. Zhang, Y. Chen, Y. Hei, S. Wang, Y. Shi, F. Jiang and L. Luo, Design and controllable synthesis of C-doped Bi_2O_3 nanowires with superior performance for removal of bisphenol A, *Mater. Sci. Semicond. Process.*, 2021, **132**, 105875.

34 Q. Tang, Z. Sun, S. Deng, H. Wang and Z. Wu, Decorating g-C_3N_4 with alkalinized Ti_3C_2 MXene for promoted photocatalytic CO_2 reduction performance, *J. Colloid Interface Sci.*, 2020, **564**, 406–417.

35 C. Cao, J. Yang, S. Yan, W. Bai, Y. Ma, Y. Xue and C. Tang, Photoelectric and magnetic properties of boron nitride nanosheets with turbostratic structure and oxygen doping, *2D Mater.*, 2021, **9**, 015014.

36 X. Liu, Y. Kang and Y. Wang, Novel high-efficiency visible-light-driven p–n heterojunction β-Bi_2O_3/Ag_2WO_4 photocatalysts, *Chem. Phys. Lett.*, 2022, **790**, 139347.

37 X. Li, B. Kang, F. Dong, Z. Zhang, X. Luo, L. Han, J. Huang, Z. Feng, Z. Chen, J. Xu, B. Peng and Z. L. Wang, Enhanced photocatalytic degradation and H_2/H_2O_2 production performance of S-pCN/$WO_{2.72}$ S-scheme heterojunction with appropriate surface oxygen vacancies, *Nano Energy*, 2021, **81**, 105671.

38 L. Kaur, P. Sethi and S. Basu, Rice husk biochar-boosted BiOCl nanoplates: a sunlight-responsive route to wastewater detoxification and pathway insights for methylene blue degradation, *Mater. Adv.*, 2026, **7**, 3747–3760.

39 C. Wu, H. Zuo, H. Du, S. Zhang, L. Wang and Q. Yan, Construction of layered embedding dual Z-Scheme $Bi_2O_2CO_3$/g-C_3N_4/Bi_2O_3: Tetracycline degradation pathway, toxicity analysis and mechanism insight, *Sep. Purif. Technol.*, 2022, **282**, 120096.

40 T. Yan, Z. Du, J. Wang, H. Cai, D. Bi, Z. Guo, Z. Liu, C. Tang and Y. Fang, Construction of 2D/2D Bi_2WO_6/BN heterojunction for effective improvement on photocatalytic degradation of tetracycline, *J. Alloys Compd.*, 2022, **894**, 162487.

41 S. Huang, G. Wang, J. Liu, C. Du and Y. Su, A novel $CuBi_2O_4$/BiOBr direct z-scheme photocatalyst for efficient antibiotics removal: Synergy of adsorption and photocatalysis on degradation kinetics and mechanism insight, *ChemCatChem*, 2020, **12**, 4431–4445.

42 M. Abinaya, K. Govindan, M. Kalpana, K. Saravanakumar, S. L. Prabavathi, V. Muthuraj and A. Jang, Reduction of hexavalent chromium and degradation of tetracycline using a novel indium-doped Mn_2O_3 nanorod photocatalyst, *J. Hazard. Mater.*, 2020, **397**, 122885.

43 G. C. Zhang, J. Zhong, M. Xu, Y. Yang, Y. Li, Z. Fang, S. Tang, D. Yuan, B. Wen and J. Gu, Ternary $BiVO_4$/NiS/Au nanocomposites with efficient charge separations for enhanced visible light photocatalytic performance, *Chem. Eng. J.*, 2019, **375**, 122093.

44 H. Cai, J. Wang, Z. Du, Z. Zhao, Y. Gu, Z. Guo, Y. Huang, C. Tang, G. Chen and Y. Fang, Construction of novel ternary $MoSe_2$/ZnO/p-BN photocatalyst for efficient ofloxacin degradation under visible light, *Colloids Surf., A*, 2023, **663**, 131050.

45 M. Li, J. Zhou, R. Di, Z. Zhang, X. Mu, X. Wang, Y. Gu, L. Su, J. Liu, C. Liu, C. Yuan and L. Miao, Piezoelectric potential activated interfacial electric field in $BiFeO_3$@$BaTiO_3$ heterojunction for rapid and round-the-clock photocatalytic degradation of organic pollutants, *J. Adv. Ceram.*, 2024, **13**, 2030–2042.

46 P. Sethi, S. Barman and S. Basu, Eco-friendly tetracycline remediation using robust and highly reusable ZIF-67/g-C3N4 nanocomposites with coupled adsorption and photocatalytic pathways: A deep dive into isotherms, kinetics, thermodynamics, and degradation pathways, *ACS Sustainable Resour. Manage.*, 2025, **3**, 244–259.